The Structural Compactness of a Tropical Cyclone Seed Affects Its Persistence

KUAN-YU LU,[a] DANIEL R. CHAVAS,[a] AND DANYANG WANG[a]

[a] *Department of Earth, Atmospheric, and Planetary Sciences, Purdue University, West Lafayette, Indiana*

(Manuscript received 11 September 2023, in final form 6 August 2024, accepted 2 September 2024)

ABSTRACT: Tropical cyclones (TCs) are often generated from preexisting "seed" vortices. Seeds with higher persistence might have a higher chance to undergo TC genesis. What controls seed persistence remains unclear. This study proposes that planetary Rossby wave drag is a key factor that affects seed persistence. Using recently developed theory for the response of a vortex to the planetary vorticity gradient, a new parameter given by the ratio of the maximum wind speed (V_{max}) to the Rhines speed at the radius of maximum wind (R_{max}), here termed "vortex structural compactness" (C_v), is introduced to characterize the vortex weakening by planetary Rossby wave drag. The relationship between vortex compactness and weakening rate is tested via barotropic β-plane experiments. The vortex's initial C_v is varied by systematically varying their initial V_{max} and R_{max} in idealized wind profile models. Experiments are also conducted with real-world seed vortices from reanalysis data, which possess natural compactness variability. The weakening rate depends strongly on the vortex's initial C_v across both idealized and real-world experiments, and the initial axis-asymmetry introduces minor differences. Experiments doubling the size of seed vortices cause them to weaken more rapidly, in line with other experiment sets. The dependence of the weakening rate on initial compactness can be predicted from a simple theory, which is more robust for more compact vortices. Our results suggest that a seed's structure strongly modulates how long it can persist in the presence of a planetary vorticity gradient. Connections to real seeds on Earth are discussed.

SIGNIFICANCE STATEMENT: This study explores the evolution of tropical cyclone (TC) seeds, which are preexisting weakly rotating rainstorms, in a simple setting that isolates the dynamical effects of the rotating sphere. It is not clear why some seeds can persist for a longer duration and might have a higher chance to eventually undergo genesis. We proposed that a factor called "planetary Rossby wave drag" plays a crucial role in this process. To investigate this, we introduce a new parameter called "compactness" to describe how the size and intensity of a seed vortex determines how quickly it will weaken due to this drag. We conducted experiments with numerical simulations and real-world TC seeds to test our ideas. Our findings show that the initial compactness of seeds strongly influences how quickly they weaken. We have developed a formula to predict how quickly these seeds weaken based on their compactness, which is especially accurate for more compact seeds. This research helps us understand how planetary Rossby wave drag affects the persistence of a TC seed and, ultimately, how it might impact the frequency of TCs.

KEYWORDS: Barotropic flows; Rossby waves; Tropical cyclones

1. Introduction

Tropical cyclones (TCs) are one of the most devastating natural disasters on Earth. These intense rotating storms can cause significant damage to coastlines and populations in their path (Rappaport 2014; Emanuel 2005). Given that the frequency of TCs—defined as the occurrence counts of TCs within a specified time window and geographical domain—directly controls the overall level of hazard and risk associated with TCs, comprehending the frequency and genesis processes of TCs becomes crucial for predicting and mitigating their impacts (Sobel et al. 2021).

Theoretically, TCs can form spontaneously in certain rotational radiative–convective equilibrium (RCE) simulations with convectively favorable environments and initial small-amplitude random thermal noise (e.g., Nolan et al. 2007; Held and Zhao 2008; Wing et al. 2016; Cronin and Chavas 2019). However, observational studies have revealed that the majority of TCs originate from preexisting precursor disturbances, such as the intertropical convergence zone (ITCZ) breakdown (Cao et al. 2013; Kieu and Zhang 2008) or African easterly waves (AEWs) (Thorncroft and Hodges 2001; Russell et al. 2017). These precursor disturbances are often referred to as TC "seeds." Recent research proposes a seeding-transition framework to interpret TC genesis variability across different climatologies (Hsieh et al. 2020; Vecchi et al. 2019). This framework involves the transformation of a tropical convective cluster into a seed and the development of a seed into a TC. The length of the seeding stage defines the persistence of seeds. If a seed manages to persist and encounters a favorable thermodynamic environment (i.e., low ventilation) before dissipation, it may have a higher chance of undergoing genesis and developing into a TC (Hoogewind et al. 2020; Hsieh et al. 2020; Tang and Camargo 2014; Vecchi et al. 2019). In previous studies (e.g., Hopsch et al. 2010; Ikehata and Satoh 2021), the main focus has been on the transition probability from seeds to TCs, with relatively less attention given to the duration of the seeding stage. Moreover, past investigations (Lee et al. 2020; Hsieh et al. 2020; Vecchi et al. 2019; Yamada et al. 2021; Sugi et al. 2020) have primarily concentrated on the influence of environmental factors on seed development, absolute

Corresponding author: Kuan-Yu Lu, kuanyulu.as@gmail.com

DOI: 10.1175/JAS-D-23-0149.1

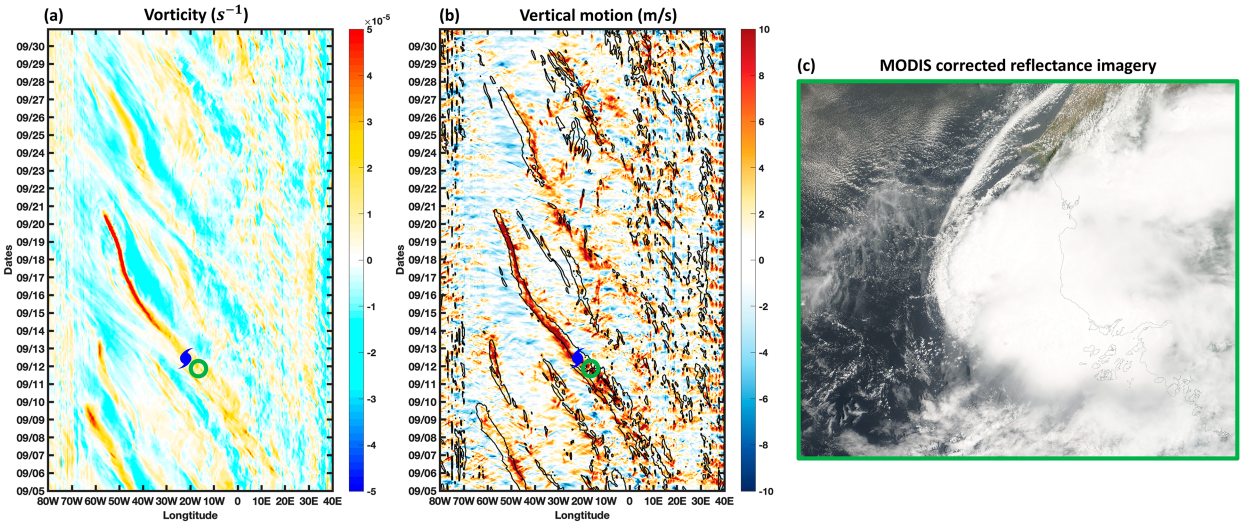

FIG. 1. An example of AWEs that generate TC seeds. (a) The Hovmöller diagram illustrates the evolution of ERA5 850-hPa relative vorticity averaged between 5° and 15°N. The blue cyclone symbol represents the genesis of Hurricane Helene (2006). (b) As in (a), but for the average vertical motion between 1000 and 500 hPa. Black contours indicate an averaged 850-hPa relative vorticity greater than 10^{-5} s^{-1}. (c) A MODIS corrected reflectance satellite image of Hurricane Helene's seed. The satellite image was downloaded from NASA EOSDIS Worldview. The location and time of this snapshot are indicated by the green circle in both (a) and (b).

counts, and transition probability. However, there has been limited inquiry into how the structure and dynamics of the seed itself affect its persistence.

Theoretically, seed persistence can affect the frequency of TCs in two ways. First, a seed that persists for a longer duration has a higher probability of encountering an environment favorable for the genesis of TCs, assuming the climatology of the ventilation index remains unchanged. Second, increasing the overall persistence of seeds contributes to higher seed counts at any given point during the TC season. Consequently, even if the generation rate remains constant, the annual frequency of TCs may still increase due to the augmented number of seeds. Therefore, investigating the dynamics of seed persistence can lead to a more comprehensive understanding of TC frequency.

As mentioned previously, TC seeds typically originate from a variety of larger-scale dynamical phenomena. For instance, in the North Atlantic basin, AEWs serve as the primary source of TC seeds (Thorncroft and Hodges 2001; Russell et al. 2017). Figure 1 illustrates the AEW seed of Hurricane Helene (2006) along with other nearby AEWs, the latter of which are all potential (but nondeveloping) TC seeds that persist for varying durations. The figure suggests that even seeds originating from the same larger-scale dynamical phenomenon around a similar time can exhibit different persistence, and there is limited discussion of this variability.

The meridional variance in the Coriolis parameter on Earth is commonly denoted as β. Recently, Lu and Chavas (2022, hereafter LC22) proposed that the size of a TC-like vortex on a barotropic β plane is constrained by the vortex Rhines scale (R_{VRS}). Specifically, circulations larger than R_{VRS} dissipate rapidly due to the influence of planetary Rossby waves, while circulations within R_{VRS} remain largely unaffected and maintain axisymmetry. Note that in this study, the term "planetary Rossby waves" does not refer to Rossby waves that have a planetary scale but specifically to those Rossby waves stimulated by the planetary vorticity gradient, β. LC22's primary focus was on examining the size of mature TC-like vortices, which typically possess the strongest circulation located well within R_{VRS}. The impact of planetary Rossby waves on vortex intensity remains uncertain when the strongest circulation of a vortex is situated near or even outside R_{VRS}.

In this study, we are proposing the following research questions:

1) How do planetary Rossby waves affect the intensity of an individual seed vortex?
2) Does the structure of the vortex affect the vortex intensity response to planetary Rossby waves?

To answer these questions, section 2 will begin by revisiting the Rhines effect as proposed in LC22 and subsequently establish a novel structural parameter to characterize the influence of planetary Rossby waves on vortex intensity. Next, section 3 will demonstrate the model configuration, data processing, and experimental designs employed in this study. The results and analyses of our experimental sets will be presented in section 4. Finally, section 5 will provide a summary of our key findings, along with a discussion of the implications arising from our results.

2. Theoretical background

a. *Planetary Rossby wave drag, Rhines number, and dynamical pouch*

The essence of a TC seed is simply a rotating convective cluster, and its development can be expressed by a low-level vorticity equation for flow above the boundary layer, away

from friction (Hsieh et al. 2020; Raymond and López Carrillo 2011; Haynes and McIntyre 1987):

$$\frac{d\zeta}{dt} = (-\delta)(f + \zeta) - (\beta + \partial_y \overline{\zeta})v + \varepsilon, \tag{1}$$

where ζ represents the relative vertical vorticity, f denotes the Coriolis parameter, $\overline{\zeta}$ is the environmental (background mean) vorticity, δ stands for horizontal divergence, β represents the meridional gradient of f, ∂_y is the meridional gradient operator, v is the meridional wind, and ε is the small-scale vorticity forcing term such as the baroclinic generation term. The physical meaning of the first term on the left-hand side (LHS) is the Lagrangian tendency (following the vortex) of relative vertical vorticity. The first term on the right-hand side (RHS) represents the stretching term of absolute vorticity. The second term on the RHS includes the meridional advection of planetary vorticity ($-\beta v$) and environmental vorticity ($-\partial_y \overline{\zeta} v$), whose sum is often referred to as the effective β term.

A typical TC seed is characterized by cyclonic rotation and active convection, leading to a low-level convergence. As a consequence, the stretching term within a TC seed typically acts as a vorticity source term. On the other hand, the effective β (i.e., the meridional gradient of absolute vorticity), represented by $\beta + \partial_y \overline{\zeta}$ [the second term on the rhs of Eq. (1)], provides a background meridional vorticity gradient, stimulating planetary Rossby waves and decreasing vorticity through wave drag effects. Therefore, this β term physically represents planetary Rossby wave drag, and it is crucial for understanding the evolution of seed intensity. It is important to note that the focus of this work is on comprehending the role of the sink term (planetary Rossby wave drag) in the seed's intensity evolution. Considering the source term will be a natural progression for future research.

Unlike the typical wave drag experienced by a sailing boat or human swimming, which dissipates linear momentum by generating gravity waves (Vorontsov and Rumyantsev 2000; Wilson and Thorp 2003; Vennell et al. 2006; Yang et al. 2013), planetary Rossby wave drag dissipates angular momentum by generating planetary Rossby waves, thus decelerating the circulation of a vortex. Furthermore, planetary Rossby wave drag is not radially homogeneous within a vortex. To demonstrate the radial dependence of planetary Rossby wave drag within a vortex, we adopt a 2D barotropic vorticity equation, which is the simplest model that allows for the consideration of planetary Rossby wave drag. By setting $\delta = 0$, omitting ε, assuming $\partial_y \overline{\zeta} = 0$, and only considering horizontal components in Eq. (1), we can obtain the 2D barotropic vorticity equation:

$$\frac{\partial \zeta}{\partial t} = -\mathbf{u} \cdot \nabla \zeta - \beta v, \tag{2}$$

where $\mathbf{u}$ represents the horizontal wind field. In Eq. (2), the LHS is the vorticity Eulerian tendency term. The first term on the RHS is the nonlinear vorticity advection term, and the second term represents the β term.

When the β term dominates the vorticity tendency in Eq. (2), it stimulates planetary Rossby waves. To express the relationship between β term and the nonlinear advection term within a vortex, LC22 defines the ratio between these two terms as the Rhines number, Rh. By converting the coordinate into a cylindrical form, applying scale analysis and β-plane approximation to Eq. (2), Rh can be written as follows:

$$\frac{\mathbf{u} \cdot \nabla \zeta}{\beta v} \equiv \mathrm{Rh} = \frac{U_t}{2\pi\beta r^2}. \tag{3}$$

where U_t is the tangential circulation speed of a vortex and r is the radius of the circulation. A detailed derivation is described in the appendix. When a circulation has a faster speed (stronger U_t) or a smaller size (smaller r), it results in a larger Rh value ($\mathrm{Rh} \gg 1$). This indicates that the circulation is not dominated by the β term and can circulate without a significant amount of planetary Rossby wave drag on it. On the other hand, if circulation is slower (has a smaller U_t) or has a larger size (larger r), it results in a smaller Rh value ($\mathrm{Rh} \ll 1$), indicating that the circulation is dominated by the β term and is significantly decelerated by planetary Rossby wave drag.

As demonstrated in LC22, we may define the Rhines speed, U_{Rh}, by setting $\mathrm{Rh} = 1$ in Eq. (3) and solving for U_t, resulting in

$$U_{\mathrm{Rh}}(r) \equiv 2\pi\beta r^2. \tag{4}$$

The U_{Rh} profile (red dashed curve in Fig. 2a) on a β plane is fixed because it depends solely on r and β, and β is constant on a β plane. For a circulation with a known size, U_{Rh} represents a transition speed that determines the significance of planetary Rossby wave drag. That is, planetary Rossby wave drag is strong when $U_t < U_{\mathrm{Rh}}$ and is weak when $U_t < U_{\mathrm{Rh}}$. In LC22, the radius of the intersection between U_{Rh} and U_t profiles is defined as the vortex Rhines scale (R_{VRS}), depicted as the black solid vertical line in Fig. 2a. Analogous to the concept of a "thermodynamic pouch" proposed by Dunkerton et al. (2009), we refer to the region within R_{VRS} as the "dynamical pouch" (highlighted in the shaded region in Fig. 2a). Within this dynamical pouch, the circulation speed is faster than U_{Rh}, and it is expected to be "protected" from the influence of planetary Rossby wave drag. However, although we can mathematically define a clear boundary for the dynamical pouch, it should be viewed physically as a transition zone between the inner pouch region and the outer wave drag region. Furthermore, the dynamical pouch concept shares certain similarities with Kelvin's cat's eye theory, which is characterized as a closed contour of potential vorticity (Asaadi et al. 2016a,b, 2017) or streamfunction (Dunkerton et al. 2009). Both frameworks describe a region at small radii where nonlinearity dominates the flow evolution, yielding a persistent recirculating regime. Kelvin's cat's eye focuses on the process of axisymmetrization within this region, and further note that such disturbances are more persistent when the meridional potential vorticity gradient is weak. Our theory quantifies the planetary Rossby wave drag on the vortex circulation and defines a radius within which the effect of wave drag is small. These theories are consistent and highly complementary, as

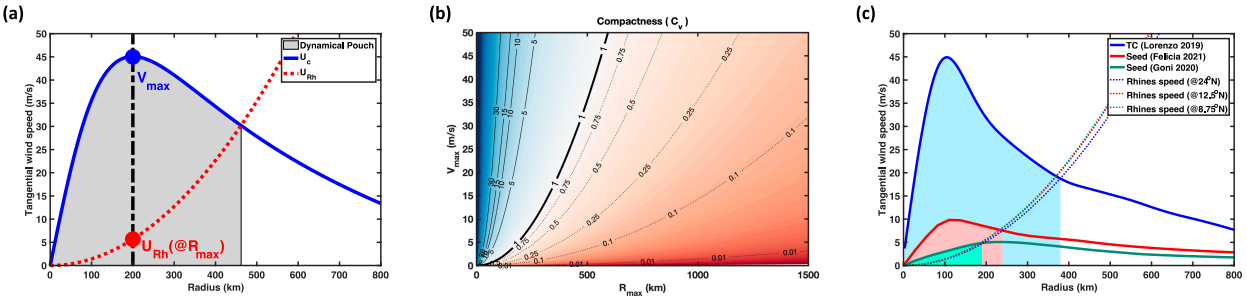

FIG. 2. A comprehensive visualization of the definition of C_v, the dynamical pouch, variations in C_v, and three example wind profiles with different C_v values. (a) The conceptual diagram illustrates the definition of C_v and the dynamical pouch for an example wind profile. The blue curve represents the azimuthal averaged tangential wind profile of an idealized mature TC-like vortex, while the red dashed curve indicates the U_{Rh} profile when $\beta = \beta(@10°\mathrm{N})$. The gray shading area indicates the region of the dynamical pouch, which is the region of the vortex lying inside R_{VRS} (depicted by the black solid vertical line). (b) The conceptual diagram illustrates C_v corresponding to different $V_{\max}$ and $R_{\max}$. Warmer colors indicate larger C_v, while colder colors represent smaller C_v. The black curves are the contours of C_v, with solid curves indicating $C_v > 1$ and dashed curves indicating $C_v < 1$. (c) The tangential wind profiles of an example mature TC (blue), an example compact seed (red), and an example incompact seed (green). The mature TC structure is obtained from the ERA5 850-hPa relative vorticity of Hurricane Lorenzo (2019) at its lifetime peak intensity. The compact seed corresponds to the seed of Hurricane Felicia (2021), and the incompact seed corresponds to the seed of Typhoon Goni (2020). Both seeds are obtained at their lifetime peak intensity. Solid curves represent their tangential wind profiles, and dashed curves represent their corresponding U_{Rh} profiles. The dynamical pouch region of each vortex is indicated by different colored shading.

they both ultimately seek to explain why the outward eddy flux of vorticity is small inside of a threshold radius via different mechanistic pathways. Our theory offers a useful practical benefit that the threshold radius is very simple to define from operationally relevant parameters as discussed below. Our theory could also readily be generalized to include the meridional relative vorticity gradient in future work; here, we focus on the planetary vorticity gradient (β) given our simple modeling framework.

LC22 investigated this theory within the framework of strong mature TC-like vortices where their azimuthally averaged maximum wind speed ($V_{\max}$) is significantly larger than U_{Rh} at the radius of $V_{\max}$ ($R_{\max}$), resulting in planetary Rossby wave drag primarily affecting the outer circulation and constraining storm size while maintaining a steady $V_{\max}$. In this study, our focus is on weaker seed vortices that do not meet this criterion, potentially leading to more planetary Rossby wave drag on $V_{\max}$ and hence weakening of the seed vortex, due to the influence of planetary Rossby wave drag.

b. *Structural compactness*

A seed vortex typically exhibits a lower $V_{\max}$ and/or a larger $R_{\max}$. When these conditions are met, the seed's $V_{\max}$ is not significantly larger or can even be smaller than U_{Rh} at $R_{\max}$. As a consequence, the vortex's intensity is no longer distinctly protected by the dynamical pouch, and the impact of planetary Rossby wave drag on the seed's $V_{\max}$ becomes a significant consideration. To precisely quantify the effect of planetary Rossby wave drag on the vortex's intensity, we introduce the concept of vortex structural compactness, denoted as C_v. This structural parameter characterizes the ratio between $V_{\max}$ and U_{Rh} at $R_{\max}$:

$$C_v \equiv \mathrm{Rh}(@R_{\max}) = \frac{V_{\max}}{U_{\mathrm{Rh}}(@R_{\max})} = \frac{V_{\max}}{2\pi\beta R_{\max}^2}. \qquad (5)$$

Figure 2a provides a visual representation of the definition of C_v. Importantly, C_v varies with both $V_{\max}$ and $R_{\max}$. As illustrated in Fig. 2b, a vortex characterized by a stronger $V_{\max}$ and/or a smaller $R_{\max}$ has a compact structure ($C_v \gg 1$). On the other hand, a vortex with a weaker $V_{\max}$ and/or a larger $R_{\max}$ has an incompact structure ($C_v \ll 1$). Moreover, when the vortex possesses multiple local maxima of U_t values, C_v solely accounts for the maximum that yields the highest C_v. It is also essential to note that the transition region near the $C_v = 1$ contour in Fig. 2b emphasizes the absence of a distinct boundary between compact and incompact structures.

Figure 2c shows the tangential wind profiles of three example vortices obtained from the fifth major global reanalysis produced by ECMWF (ERA5): Hurricane Lorenzo (2019) as an example mature TC, the seed of Hurricane Felicia (2021) as an example compact seed, and the seed of Typhoon Goni (2020) as an example incompact seed. For the mature Hurricane Lorenzo (blue curve in Fig. 2c), its $V_{\max}$ is significantly greater than U_{Rh} at $R_{\max}$, resulting in a highly compact structure ($C_v = 28.9$). Consequently, the intensity of Hurricane Lorenzo is not expected to be significantly affected by planetary Rossby wave drag. Note that the inner core of Hurricane Lorenzo is certainly under-resolved in ERA5, but this does not alter our interpretation.

In comparison, the seed of Hurricane Felicia (red curve in Fig. 2c) exhibits a much weaker $V_{\max}$ and a similar $R_{\max}$, resulting in a relatively smaller $C_v = 5.7846$, although it still exceeds 1. Consequently, the seed vortex of Hurricane Felicia is classified as a compact seed ($C_v > 1$), but it is expected to experience a greater weakening due to planetary Rossby wave drag compared to Hurricane Lorenzo. On the other hand, the seed of Typhoon Goni displays the weakest $V_{\max}$ and the largest $R_{\max}$ among these three profiles, resulting in the smallest $C_v = 0.73$, which falls even below 1 (green curve in Fig. 2c). Therefore, the seed of Typhoon Goni is anticipated to be

subjected to the most substantial influence of planetary Rossby wave drag on its intensity when compared to the other two compact vortices.

We would like to emphasize that our theory does not provide an explanation for the specific factors influencing a vortex's value of C_v (i.e., how the vortex and its specific structure formed in the first place). Its sole purpose is to describe the impact of planetary Rossby wave drag on the vortex's intensity. Furthermore, the derivation of C_v is based on the barotropic β-plane assumption and does not consider the vorticity source term due to stretching or other factors, as our focus lies in understanding the role of the sink term (planetary Rossby wave drag) acting alone. Therefore, while C_v directly represents the influence of planetary Rossby wave drag on V_{max}, it cannot solely determine the intensity tendencies of vortices in real-world scenarios.

c. Hypothesis

According to our theory, C_v governs planetary Rossby wave drag on V_{max}, thereby directly influencing the weakening of a vortex due to planetary Rossby wave drag. To investigate the impact of C_v on vortex intensity, as well as its effect on the persistence of TC seed vortex, we propose the following hypothesis: a more compact vortex (a higher C_v) will experience a slower weakening on a barotropic β plane. We will test this hypothesis by conducting experiments using a barotropic β-plane model. The model will be initialized with idealized axisymmetric vortex models and real-world seed vorticity structures obtained from reanalysis data.

3. Methods

a. Barotropic model

To examine the isolated impact of planetary Rossby wave drag on the vortex intensity, we employ a barotropic β-plane model developed by James Penn and Geoffrey K. Vallis (available at https://empslocal.ex.ac.uk/people/staff/gv219/codes/barovort.html). This model exclusively incorporates planetary Rossby waves as a vorticity sinking process, with no inclusion of any source term. The model utilizes a pseudospectral method to solve Eq. (2) in 2D space. The pseudospectral method employs analytic derivatives to calculate horizontal winds, which are then used to evaluate nonlinear advection terms in Eq. (2). The model has 500 grid points in both the x and y directions, with a grid spacing of 20 km. The initial time step is set at 60 s, and the model also employs an adaptive time step to meet the Courant–Friedrichs–Lewy (CFL) condition. There is no external forcing applied in any of our experiments. To ensure numerical stability, the model employs a dissipation process known as the high wavenumber Smith filter (Smith et al. 2002). This filter damps any structures with wavenumbers exceeding 30.

It is important to note that the barotropic model employed in this study is two-dimensional and nondivergent. Consequently, it does not account for the azimuthally averaged radial flow and vertical motions typically observed in a real convective TC seed. As a result, the barotropic model neglects the azimuthal-mean radial mass transport while still allowing for eddies to radially transport momentum. By doing so, the model can effectively simulate the vortex response to planetary Rossby wave drag while minimizing interactions across different radii within the vortex. Accounting for the role of inflow and the vorticity source term (stretching) is a critical next step in future work. Last, we utilize the centroid of vorticity as a tracking metric to determine the vortex center over time. By employing this center, we calculate the azimuthally averaged radial profiles of tangential wind for every experiment.

b. Idealized wind field models

To achieve varying levels of structural compactness while maintaining physical consistency in the generated vortices, we employ idealized wind field models that allow us to modify the V_{max} and R_{max} of an axisymmetric vortex. Furthermore, to assess the sensitivity of our hypothesis to the choice of a wind field model, we test two distinct idealized wind field models: the C15 model and a modified Rankine vortex model, specifically for the radial profile of the vortex's azimuthal wind. First, we use the C15 model (Chavas et al. 2015; Chavas 2022) for the complete radial profile of the TC low-level tangential wind field to initialize the barotropic model. The C15 model allows us to define the wind profile using a limited set of storm and environmental parameters. The storm parameters include V_{max}, R_{max}, and the Coriolis parameter (f). The environmental parameters encompass the radiative-subsidence rate (w_{cool}), the surface drag coefficient (C_d) for the outer region, and the ratio of surface coefficients of enthalpy and drag (C_k/C_d). In this study, we fixed $f = f(@10°) = 2.5325 \times 10^{-5}$ s^{-1}, $w_{cool} = 0.002$ m s^{-1}, $C_d = 0.0015$, $C_k/C_d = 1$, $C_{dvary} = 0$ (C_d in the outer region is constant), $C_k/C_{dvary} = 0$ (C_k/C_d in the inner region is constant), and $\text{eye}_{adj} = 0$ [use the ascending inner-region model derived by Emanuel and Rotunno (2011) for the wind profile within the eye]. By adjusting the values of R_{max} and V_{max} within the C15 model, we can generate tangential wind profiles with varying degrees of C_v. While we specifically employ a TC wind profile model in this study, it is worth mentioning that the experimental approach could theoretically be applied to any wind profile, as long as there is no significant symmetric instability.

The second idealized wind field model we test is a modified Rankine vortex model. This simplified wind profile model can effectively capture the dynamic characteristics of an actual vortex. As demonstrated in Fig. 8 of Klotzbach et al. (2022), a modified Rankine vortex model successfully represents the observed TC wind field between R_{max} and the 34-kt (1 kt $\approx$ 0.51 m s^{-1}) wind radius. Hence, we have conducted a modified Rankine vortex model, which takes the following form:

$$U_t(r) = \begin{cases} V_{max}\left(\dfrac{r}{R_{max}}\right)\left(\dfrac{R_{max}}{r}\right)^{\lambda} & \text{when} \quad r < R_{max} \\ V_{max}\left(\dfrac{r - R_0}{R_{max} - R_0}\right)\left(\dfrac{R_{max}}{r}\right)^{\chi} & \text{when} \quad r \geq R_{max} \end{cases}, \tag{6}$$

TABLE 1. Selected TCs' information from IBTrACS.

Basin	TC name	ISO time	Initial latitude	Initial longitude
Northern Indian	Amphan	0600:00 UTC 15 May 2020	9.5°N	87.5°E
Eastern Pacific	Douglas	0000:00 UTC 20 Jul 2020	14.7°N	118.8°W
Northern Atlantic	Eta	1800:00 UTC 31 Oct 2020	14.9°N	72.4°W
Northern Indian	Gati	1200:00 UTC 20 Nov 2020	11.2°N	62.6°E
Western Pacific	Goni	0600:00 UTC 25 Oct 2020	10.6°N	143.9°E
Western Pacific	Haishen	1200:00 UTC 30 Aug 2020	24.9°N	145.5°E
Northern Atlantic	Laura	0000:00 UTC 20 Aug 2020	14.4°N	47.3°W
Eastern Pacific	Marie	1200:00 UTC 27 Sep 2020	12.4°N	100.4°W
Western Pacific	Maysak	0000:00 UTC 26 Aug 2020	12.8°N	133.9°E
Western Pacific	Vamco	0000:00 UTC 8 Nov 2020	8°N	134.9°E
Western Pacific	Chanthu	0600:00 UTC 5 Sep 2021	12.4°N	140.5°E
Eastern Pacific	Felicia	0000:00 UTC 17 Jul 2021	13.5°N	110.6°W
Northern Atlantic	Grace	0600:00 UTC 13 Aug 2021	15°N	46.7°W
Northern Atlantic	Ida	1200:00 UTC 26 Aug 2021	16.5°N	78.9°W
Eastern Pacific	Linda	1200:00 UTC 9 Aug 2021	12.1°N	98.2°W
Western Pacific	Mindulle	0600:00 UTC 22 Sep 2021	10.8°N	150°E
Western Pacific	Nyatoh	1200:00 UTC 28 Nov 2021	11.2°N	146.2°E
Western Pacific	Rai	1200:00 UTC 11 Dec 2021	5.3°N	145°E
Northern Atlantic	Sam	1800:00 UTC 22 Sep 2021	10°N	33.1°W
Western Pacific	Surigae	1200:00 UTC 11 Apr 2021	5.5°N	143.8°E

where λ sets the radial increasing rate of tangential winds within R_{max}, χ represents the radial decreasing rate of tangential winds outside R_{max}, and R_0 is the radius of vanishing wind [$U_t(R_0) = 0$]. Note that this modified Rankine model generates tangential wind profiles with different V_{max} and R_{max} while holding R_0 fixed. In this study, we arbitrarily set R_0 = 1500 km, $\lambda = 0.2$, and $\chi = 0.5$ in every Rankine vortex.

c. TC seeds from reanalysis

The dynamical structure of selected TC seeds is obtained from ERA5. Table 1 lists 20 selected TC cases, all of which are category 3, 4, and 5 storms sampled in 2020 and 2021 across all basins. To begin, we determine the ending time and location of each seed track using the corresponding TC's first best track data from the International Best Track Archive for Climate Stewardship (IBTrACS) (Knapp et al. 2010). Next, we backtrack the vorticity center of the TC seed hourly for 2 days by identifying the local maximum of relative vorticity at 850 hPa in ERA5. A TC seed track is defined when detected vorticity maxima are less than 1.25° apart. To exclude extratropical storms, we disregard all tracks located poleward of 30° latitude. The 2D dynamical structure of the TC seed is defined as the 850-hPa relative vorticity within a range of 7.5° from the seed center in both the zonal and meridional directions. Additionally, we only consider the seed's maximum intensity structure to initialize the barotropic model. Figure 3a demonstrates an example of the detected seed vorticity structure from ERA5. This example seed features a single vorticity center surrounded by a region of positive vorticity, which is a characteristic common to most other TC seeds in this study (not shown).

To exclude adjacent systems, we apply an axisymmetricity filter based on the method proposed by Shimada et al. (2017). This filter quantifies the axisymmetric nature of the seed vorticity field across radii, yielding a parameter denoted as γ. The value of γ ranges from 0 to 1, where a higher value indicates a greater degree of axisymmetry. In the case of a seed vortex, the γ value typically decreases monotonically with increasing radius, as depicted by the orange curve in Fig. 3b. Consequently, we eliminate any vorticity structures beyond the radius where $\gamma = 0.15$ (Fig. 3c). Note that to further enhance the clarity of the γ profile, we additionally apply a moving average filter with a width of 10 data points. Figure 3c demonstrates the effectiveness of the axisymmetricity filter in successfully excluding adjacent systems while still preserving the natural asymmetry of the seed. The filtered asymmetric vortex can serve as a direct initialization for the barotropic model. Additionally, we can compute the azimuthally averaged vorticity structure (shown in Fig. 3d) to initialize the axisymmetric experimental set, which will be elaborated upon in the subsequent section.

d. Experiment design

1) *VARYRVMAX*: VARYING VORTEX'S V_{MAX} AND R_{MAX} WITH THE C15 MODEL

We begin by conducting an experimental set using the C15 model and the barotropic model to test our hypothesis. In the C15 model, we systematically vary V_{max} from 10 to 50 m s^{-1} with an interval of 10 m s^{-1} and R_{max} from 100 to 600 km with an interval of 100 km, resulting in 30 TC-like vortices with different C_v values. Note that we include vortices with V_{max} greater than 20 m s^{-1} to extend our investigation of the effect of planetary Rossby wave drag on not only seed vortices but also stronger TC-like vortices. This approach allows us to compare the effects of planetary Rossby wave drag between idealized mature TCs and seed vortices. The initial profiles of these vortices are depicted in Fig. 4a, and a vortex with a larger initial C_v value ($C_{v,0}$) is represented with a darker color. Subsequently, we convert each tangential wind profile into an axisymmetric vorticity

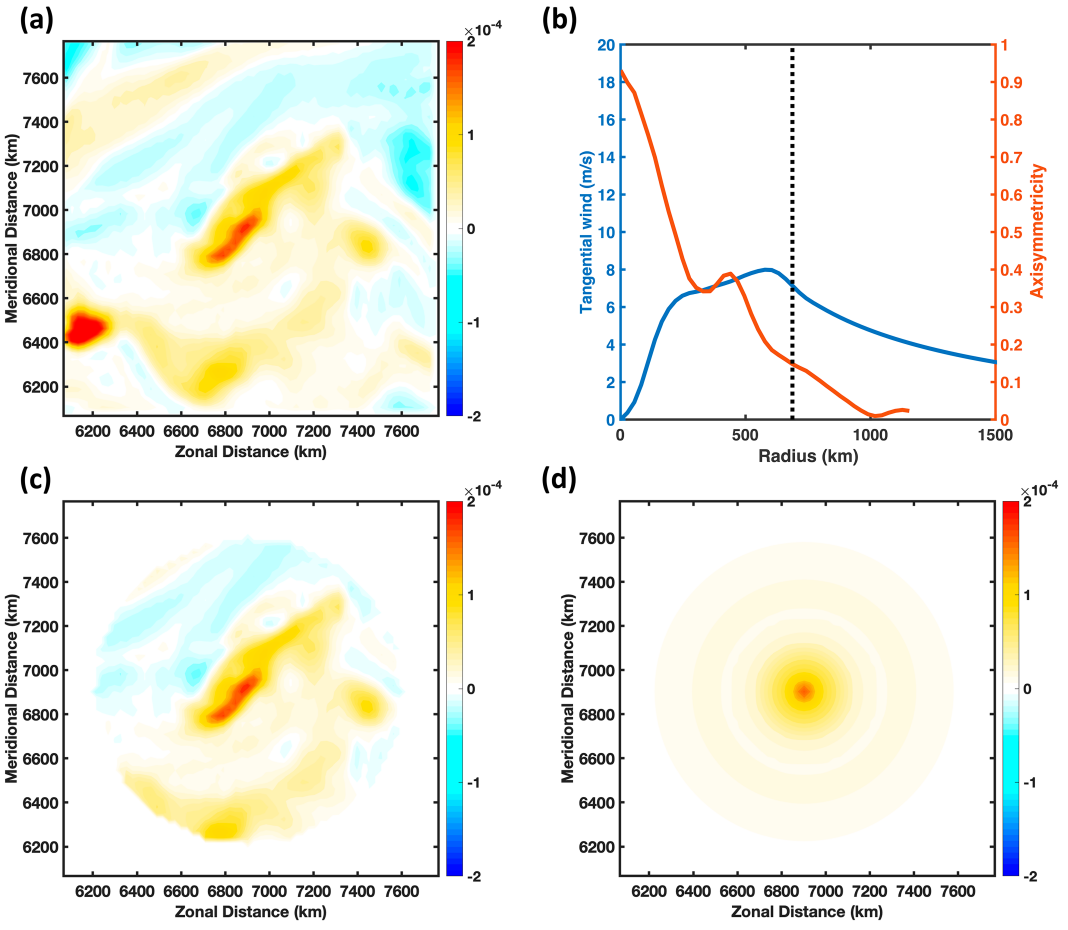

FIG. 3. A demonstration of the data processing for an example seed vortex (Cyclone Gati 2020) obtained from ERA5. (a) The 850-hPa relative vorticity field of the seed directly acquired from ERA5 at 0700 UTC 20 Nov 2020. (b) The azimuthal averaged tangential wind profile and the axisymmetricity profile of the seed. The black dashed line indicates the radius where axisymmetricity is 0.15. (c) The seed vortex after applying the axisymmetricity filter. (d) The axisymmetric vortex used for initializing *SYMSEED*, which is generated by azimuthally averaging the filtered vortex shown in (c).

field to initialize the barotropic model. The β value in the barotropic model remains fixed at $\beta(@10°\text{N}) = 2.2547 \times 10^{-11}$ m^{-1} s^{-1} across all members. Each vortex is placed at the center of the domain and simulated separately for a 1-day spinup period. Afterward, β is instantaneously turned on to the constant value for the subsequent 10 days. We then track the centroid of the vorticity in the entire domain to calculate the azimuthally averaged vortex structure. This set of experiments is labeled as *VARYRVMAX* (experiment names are italicized to aid the reader).

2) *RANKINE*: VARYING VORTEX'S V_{MAX} AND R_{MAX} WITH THE MODIFIED RANKINE VORTEX MODEL

Next, we conduct an experiment set similar to *VARYRVMAX*, but instead, we utilize the modified Rankine vortex model to generate wind profiles. Similar to *VARYRVMAX*, we systematically vary both V_{max} and R_{max} over the same range of values in the modified Rankine vortex model to create 30 vortices with different $C_{v,0}$ while keeping their R_0 constant. This set of experiments is labeled as *RANKINE* and serves to investigate whether the findings from *VARYRVMAX* remain consistent when initializing the barotropic model with a different idealized wind profile model. Figure 4b illustrates the initial profiles of all members in *RANKINE*.

3) *ASYMSEED* AND *SYMSEED*: SEED VORTICES FROM ERA5

Instead of relying solely on idealized wind profile models to specify the vortex structure, we conducted two experiment sets by initializing the barotropic model with realistic seed vortices obtained from ERA5 reanalysis data. The first experiment set, denoted as *ASYMSEED*, utilizes the asymmetric seed vortex directly extracted from ERA5. Figure 4c displays the azimuthally averaged initial wind profiles of all members in *ASYMSEED*. In the second experiment set, referred to as *SYMSEED*, the vorticity initial conditions of *ASYMSEED* are azimuthally averaged (as shown in Fig. 3d), and the barotropic model is initialized by the axisymmetric vortex with the

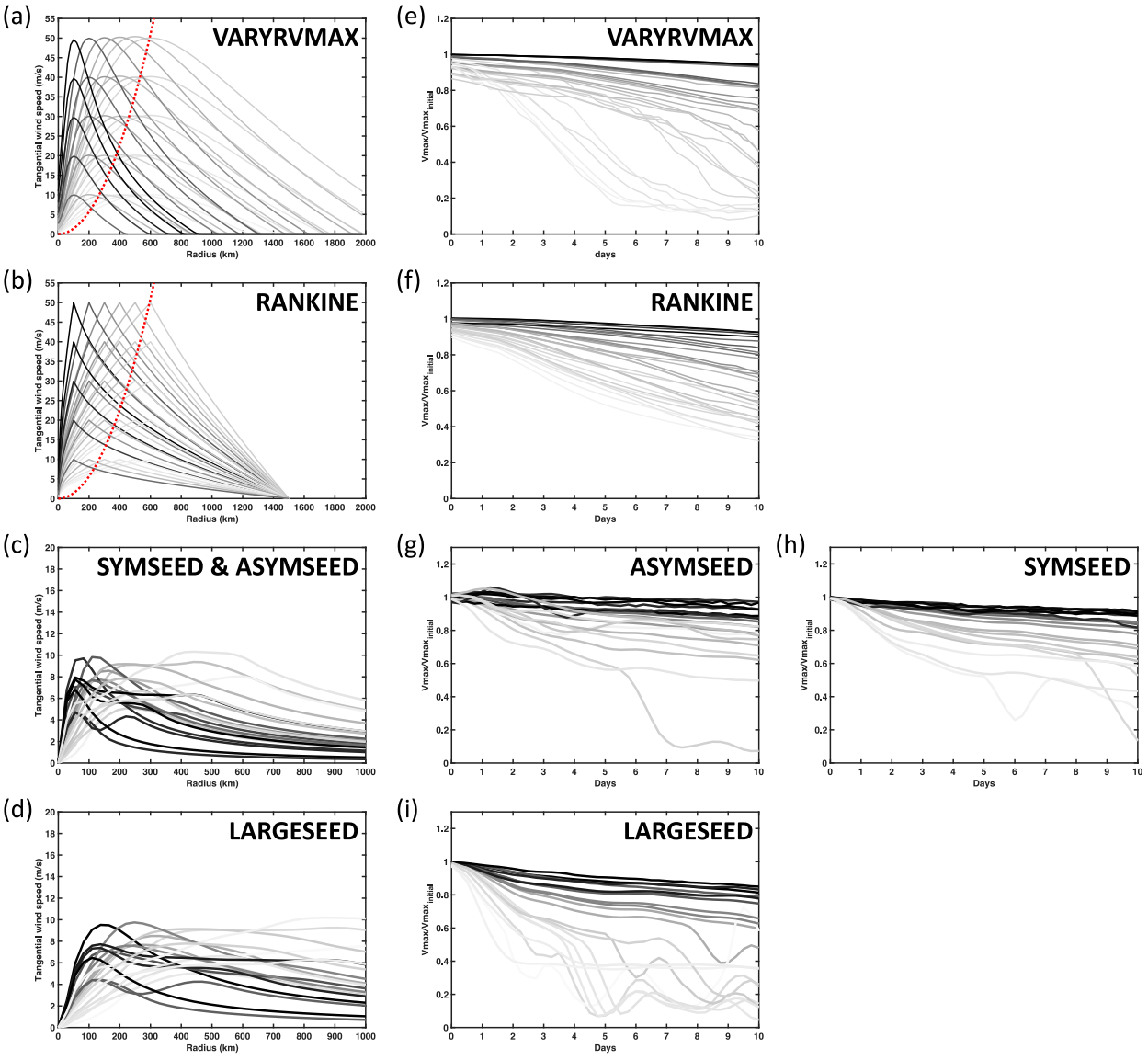

FIG. 4. The experiment designs and results of all our experiment sets. (a)–(d) The initial azimuthal averaged tangential wind profiles of all members in *VARYRVMAX*, *RANKINE*, *ASYMSEED*, and *LARGESEED*, respectively. Note that *SYMSEED* has an identical initial wind profile as *ASYMSEED*; therefore, it is not shown. (e)–(i) The normalized $V_{\max}$ evolution of all members in *VARYRVMAX*, *RANKINE*, *ASYMSEED*, *SYMSEED*, and *LARGESEED*, respectively. The gray scale indicates the $C_{v,0}$ of each member in each experiment set, with darker colors representing relatively higher $C_{v,0}$. The red dashed curves in (a) and (b) indicate U_{Rh} profiles on the corresponding β plane. Note that since all members in *SYMSEED*, *ASYMSEED*, and *LARGESEED* are simulated on different β planes, their corresponding U_{Rh} profiles are not shown in (c) and (d).

same configurations as *ASYMSEED*. Note that the azimuthal averaged initial wind profiles of *SYMSEED* (not shown) are identical to those in *ASYMSEED* (Fig. 4c).

In both *ASYMSEED* and *SYMSEED*, each experiment adjusts the β value in the barotropic model according to the latitude of the seed center while maintaining it constant throughout the entire domain and the whole 10-day simulation. Moreover, there is no spinup period in either *ASYMSEED* or *SYMSEED*. The objective of these experiment sets is to test our hypothesis using realistic seed vortices. By comparing the results between *SYMSEED* and *ASYMSEED*, we can also investigate the effect of the asymmetry feature of realistic seeds on our hypothesis.

4) *LARGESEED*: RESCALING AXISYMMETRIC SEED VORTICES FROM *SYMSEED*

Seed vortices from ERA5 naturally exhibit variability in $C_{v,0}$, but it is possible to manually decrease the vortex $C_{v,0}$ by radially enlarging the entire wind profile of an axisymmetrized seed vortex. Here, we utilize all axisymmetric members from *SYMSEED*

and enlarge their entire structure by a factor of 2. This particular experiment set is referred to as *LARGESEED*, and the initial profiles are demonstrated in Fig. 4d. The focus of *LARGESEED* is to test the hypothesis by reducing the $C_{v,0}$ of the seed while keeping the other aspects of the vortex structure unchanged.

4. Results

a. *VARYRVMAX and RANKINE*

Since each member has a different V_{max}, to standardize the comparative analysis across different members, we define the normalized intensity as $\tilde{V}_{max} = V_{max}/V_{max,0}$, where $V_{max,0}$ is the initial V_{max} of each member. Figure 4e displays the $\tilde{V}_{max}$ evolution for all members in *VARYRVMAX* after turning on β. All members immediately start weakening after the spinup period, including the most compact vortex (i.e., highest $C_{v,0}$). Overall, more compact vortices (larger $C_{v,0}$) exhibit slower rates of weakening. Some less compact vortices (smaller $C_{v,0}$) are almost entirely dissipated by planetary Rossby wave drag, with $\tilde{V}_{max}$ evolution curves fluctuating between 0 and 0.2. Figure 4f presents similar visualizations to Fig. 4e but for the *RANKINE* experiment set. Similar to *VARYRVMAX*, more compact vortices in *RANKINE* weaken slower. While those compact members have similar $\tilde{V}_{max}$ evolution across the two experiment sets, less compact vortices in *RANKINE* weaken slower than those in *VARYRVMAX*. Another difference is that there is no member in *RANKINE* that reaches a quasi-steady state during the 10 days of simulation. Results from both *VARYRVMAX* and *RANKINE* support the hypothesis, which states that a more compact vortex will experience less planetary Rossby wave drag on V_{max} and weaken slower. This suggests that our theory is not highly sensitive to the choice of the idealized wind profile model for the initial conditions.

b. *ASYMSEED, SYMSEED, and LARGESEED*

Figures 4g and 4h depict the evolution of $\tilde{V}_{max}$ for *ASYMSEED* and *SYMSEED*, respectively. The results obtained from both *ASYMSEED* and *SYMSEED* reveal that more compact vortices experience slower rates of weakening, indicating that our hypothesis is not highly sensitive to the presence of asymmetry in realistic seed vortex structures.

While all members of *SYMSEED* begin weakening immediately, certain members of *ASYMSEED* exhibit a brief period of minor intensification at the beginning of the simulation. This can be attributed to *ASYMSEED*'s initially asymmetric members, coupled with the absence of a spinup period. Consequently, the initial axisymmetrization process of certain members in *ASYMSEED* contributes to their minor intensification. In contrast, the immediate weakening observed in *SYMSEED* can be explained by its initial axisymmetric vortex, which bypasses any potential intensification resulting from axisymmetrization.

In addition, the majority of members in both *ASYMSEED* and *SYMSEED* do not weaken to a $\tilde{V}_{max}$ value below 0.4. The few members that reach values lower than 0.4 do so because their maximum vorticity weakens to a magnitude similar to the stimulated planetary Rossby wave vorticity anomalies, causing the centroid tracking algorithm to lose the vortex.

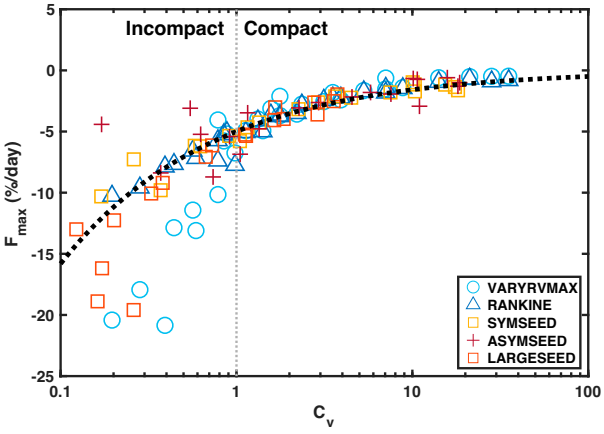

FIG. 5. The scatter plot illustrates the relationship between the weakening rate (F_{max}) and the initial structural compactness ($C_{v,0}$) of all members. The weakening rate F_{max} is defined as the linear regression slope of the normalized V_{max} evolution during the first 5 days (% day^{-1}). Members from the same experiment set are indicated by the same marker. The black dashed curve represents the fitted theoretical prediction curve.

The results obtained from both *ASYMSEED* and *SYMSEED* serve as a proof of concept for how our hypothesis applies to realistic seed structures. They both demonstrate that the $C_{v,0}$ remains a reliable indicator of how quickly the vortex will weaken due to planetary Rossby wave drag, and the inclusion of 2D realistic asymmetry does not significantly diminish the reliability of $C_{v,0}$. This is of practical use since $C_{v,0}$ can be estimated from V_{max}, R_{max}, and storm central latitude alone.

Finally, Fig. 4i illustrates the temporal evolution of $\tilde{V}_{max}$ for all members within the *LARGESEED* experiment set. The results from *LARGESEED* provide robust support for our hypothesis, revealing that by manually enlarging the *SYMSEED* members, less compact vortices weaken faster. A comparison between *LARGESEED* (Fig. 4i) and *SYMSEED* (Fig. 4h) demonstrates an overall accelerated weakening rate and more entirely dissipated members in the former. It is noteworthy that during the 10-day simulation period, most cases in *SYMSEED* do not attain a quasi-steady state or exhibit fluctuating behavior at low $\tilde{V}_{max}$ values. However, two cases in the *LARGESEED* reach a steady state, maintaining a $\tilde{V}_{max}$ around 0.4.

c. *The relationship between the $C_{v,0}$ and the weakening rates*

As demonstrated previously, all experimental sets presented in this study support our hypothesis that vortices with higher $C_{v,0}$ values will exhibit slower weakening. To further quantitatively validate this finding, we introduce the weakening rate, denoted as F_{max}, which is defined as the linear regression slope of the $\tilde{V}_{max}$ evolution during the first 5 days of the simulation. The F_{max} is expressed in units of percentage per day and represents the average daily percentage of weakening. Figure 5 presents a scatterplot illustrating the relationship

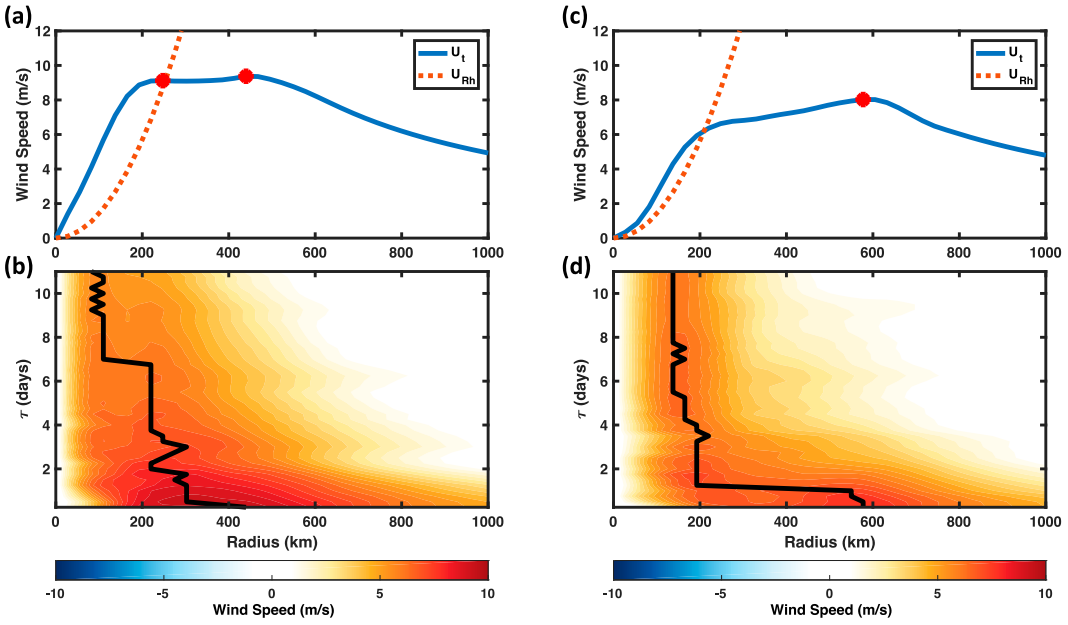

FIG. 6. A demonstration of two cases from *ASYMSEED* that both have a significant shifting in R_{max}, contributing to the deviation of actual F_{max} from the F_{max} predicted by their $C_{v,0}$. (a) Initial wind profile of the Cyclone Amphan (2020) seed. The blue curve represents U_t profile, and the brown dashed curve depicts U_{Rh} profile at the corresponding latitude. Red dots denote the detected local maxima of U_t. (b) Hovmöller diagram displaying the temporal evolution of U_t for the Cyclone Amphan (2020) seed. The contours represent U_t, while the thick black curve illustrates the progression of R_{max}. (c) As in (a), but for the seed of Cyclone Gati (2020). (d) As in (b), but for the seed of Cyclone Gati (2020).

between the $C_{v,0}$ and F_{max} values for all members across all experiment sets.

Overall, a clear positive relationship is observed between $C_{v,0}$ and F_{max}. Larger values of $C_{v,0}$ correspond to larger (less negative) values of F_{max}, indicating a slower weakening rate. Note that Fig. 5 also illustrates the distribution of $C_{v,0}$ among our seeds extracted from ERA5. Despite all being developing seeds, there is a notable variance in their structures, ranging from highly compact ($C_{v,0} \approx 20$) to distinctly incompact ($C_{v,0} \approx 0.2$). This highlights the inherent significant variability in compactness among seeds from ERA5. Furthermore, it seems that F_{max} is inversely proportional to $-C_{v,0}^{1/2}$. Consequently, an overlay of a prediction curve (indicated by the black dashed curve in Fig. 5) highlights the dependence of F_{max} on $C_{v,0}$. This prediction curve is expressed as follows:

$$F_{max} = -\alpha\sqrt{\frac{1}{C_{v,0}}}, \tag{7}$$

where α is a scaling factor that has the best-fitted value of 5.35% day^{-1} that minimizes the χ^2. This F_{max} prediction is particularly robust for the compact members across all experimental sets, as evidenced by the close fit of the experimental data to the prediction curve when $C_{v,0} > 1$. However, there are also distinct variations among the different experiment sets within those incompact members. For instance, while *VARYRVMAX* and *RANKINE* exhibit identical distributions in $C_{v,0}$, incompact members in *VARYRVMAX* weaken faster than the prediction curve. On the other hand, although *SYMSEED* and *ASYMSEED* share identical initial azimuthal wind profiles, some incompact members in *ASYMSEED* weaken slower than the prediction curve. These observations suggest that the $C_{v,0}$–F_{max} relationship is not significantly influenced by structural variance across the experiment sets when the vortex is compact. However, systematic structural differences introduce more variability and decrease the robustness of the F_{max} prediction for the incompact members across all experiment sets. Furthermore, note that the results are similar when calculating F_{max} over averaging periods spanning from 1 to 8 days (not shown).

Reasons why vortices with similar $C_{v,0}$ values but different structures display notable differences in their weakening rates (F_{max} spread) are not completely understood. One scenario that can potentially result in deviations of members' F_{max} from the theoretical prediction curve is the inward shifting of R_{max}. This shift in R_{max} may arise due to the presence of multiple local maxima of U_t for the seed or due to the seed's initial incompact structure. Figure 6a illustrates the radial wind profile of a member in the *ASYMSEED*, which initially exhibits two detected local maxima in U_t. As the inner local maximum of U_t yields a higher C_v (with similar U_t but at a smaller R_{max}), it is utilized to calculate $C_{v,0}$ for this seed. However, since the outer local maximum of U_t initially has a higher value, it is considered the V_{max} of this seed. During the first 5 days of the simulation, R_{max} rapidly shifts inward as the outer circulation, including the outer local maximum of U_t, immediately weakens due to planetary Rossby wave drag (Fig. 6b). Consequently, the predicted weakening rate (−4.9% day^{-1}) based on $C_{v,0}$ underestimates the actual weakening rate (−6.9% day^{-1}) of this seed.

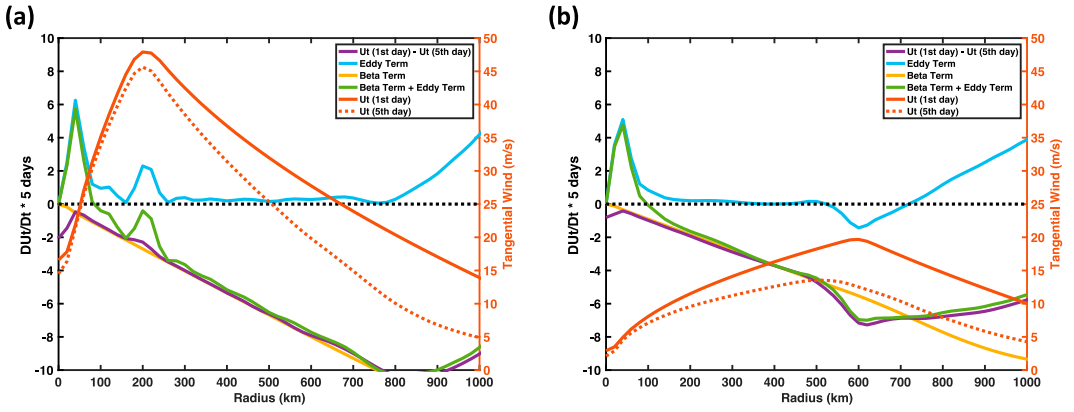

FIG. 7. Radial distribution of all terms in Eq. (8). These azimuthally averaged results are acquired from two example members. (a) A vortex from *RANKINE* which has an initial $V_{\max} = 50$ m s^{-1} at $R_{\max} = 200$ km. The solid orange curve is the initial U_t of this vortex, and the dashed orange curve is U_t at the end of the fifth day of the simulation (after turning on β). The purple curve is the total change of U_t during the first 5 days, which is the difference between the solid orange curve and the dashed orange curve. The other three curves are radial profiles of each term in Eq. (8) after integrating them for the first 5 days of the simulation, where the light blue curve is the eddy term, yellow is the β term, and green is the sum of these two terms, representing the diagnosed U_t changes. (b) As in (a), but for a vortex from *RANKINE* that has an initial $V_{\max} = 30$ m s^{-1} at $R_{\max} = 600$ km.

On the other hand, when a seed is initially incompact, as demonstrated in Fig. 6c, the initial $V_{\max}$ of the seed experiences rapid weakening due to the impact of planetary Rossby wave drag, as illustrated in Fig. 6d. Meanwhile, the inner circulation within the dynamical pouch experiences relatively less planetary Rossby wave drag. As a result, the inner circulation weakens less and thus becomes stronger than the outer $V_{\max}$. This leads to the replacement of the weakening outer $V_{\max}$ by the more persistent inner circulation as the new $V_{\max}$ throughout the remainder of the simulation. This transition is clearly depicted by the abrupt jump in $R_{\max}$ during the initial 2 days of the simulation, as shown in Fig. 6d. Since the calculation of $F_{\max}$ is based on the evolution of $\tilde{V}_{\max}$ during the first 5 days, it incorporates both the rapid weakening of the initially outer $V_{\max}$ and the more gradual weakening of the persistent inner $V_{\max}$. Consequently, the predicted weakening rate (-12.1% day^{-1}) based on $C_{v,0}$ overestimates the actual weakening rate (-4.4% day^{-1}) of this seed.

d. *Derivation of the $C_{v,0}$–F_{max} relationship*

We are in pursuit of a straightforward theoretical explanation for the tight dependence of $F_{\max}$ on $-C_{v,0}^{-1/2}$ found in our simulations. Here, we employ the horizontal component of the azimuthal mean tangential momentum budget equation on a barotropic β plane in a storm-following cylindrical coordinate (Smith et al. 1995; Persing et al. 2002). In a quiescent environment, the equation is expressed as follows:

$$\underbrace{\frac{\partial \overline{U_t}}{\partial t}}_{\text{Tendency term}} = \underbrace{-\overline{U_r'\zeta'}}_{\text{Eddy term}} \underbrace{- \beta r \overline{\sin\theta (U_r' + c_r)}}_{\text{Beta term}}, \tag{8}$$

where U_r is the radial wind, ζ is the vertical relative vorticity, r is the radius, θ is the counterclockwise azimuth angle measured from the eastward direction, and c_r is the radial component of the storm motion vector. Overbars indicate azimuthally averaged quantities, and primed quantities indicate deviations from this azimuthal average. On the LHS is the tendency of the azimuthally averaged tangential wind. On the RHS, the first term is the eddy term, and the second term is β term. Note that the mean vorticity flux ($-\overline{U_r}\,\overline{\zeta}$) is neglected since there is no azimuthal mean divergent flow in a barotropic fluid.

In Eq. (8), planetary Rossby wave drag is introduced by the β term and acts as a momentum sink. Meanwhile, the eddy term represents radial vorticity fluxes, whose effect on the tendency of U_t is complex and not directly discernible from the equation. We utilize Eq. (8) to conduct a budget analysis for U_t for one compact vortex and one incompact vortex within *RANKINE*. Given that $F_{\max}$ takes into account only the evolution of $V_{\max}$ during the initial 5 days, we will integrate the results of the budget analysis over time for this same period to ensure consistency in our examination. Figure 7a presents the time-integrated budget analysis results for the compact vortex. The diagnosed change in U_t (green curve) is calculated as the sum of the eddy term (light blue curve) and the β term (yellow curve). The actual change in U_t (purple curve) is calculated from the difference between the initial U_t profile (the solid orange curve) and the U_t profile at the end of the fifth day (the dashed orange curve). The diagnosed U_t changes closely align with the actual changes, suggesting that the budget is nearly closed, with the exception of small radii within 100 km where discrepancies arise due to the nature of the tracking algorithm used in the analysis, as well as near $R_{\max}$ likely due to the rapid fluctuations of the eddy term in the vicinity of a local maximum in velocity. U_t decreases at all radii, and this tendency is well captured by the β term, whereas the eddy term remains small and slightly positive

throughout. Hence, for the compact case, the eddy term can indeed be neglected, and the β term is dominant.

For the incompact case (Fig. 7b), the eddy term is again weaker than the β term at most radii, but it is now negative and is not negligible relative to the β term. In other words, the β term remains the dominant term in the tangential wind budget at most radii for the incompact vortex, except beyond 600 km. This outcome implies that neglecting the eddy term in the analysis of $V_{\max}$ changes for our experiments with initially incompact vortices could lead to additional variability beyond the beta term alone, which likely explains the wider variance in the simulation results about the fitted curve for $C_v < 1$ in Fig. 5.

Finally, we can apply this budget analysis specifically to vortex intensity, i.e., $R_{\max}$ and $V_{\max}$. The eddy term is poorly understood, but its effects are only significant for incompact vortices. Hence, for simplicity, we consider only the β term at $R_{\max}$ to approximate $V_{\max}$ tendency, and Eq. (8) can now be simplified as follows:

$$\frac{\partial V_{\max}}{\partial t} = -\beta R_{\max}\overline{\sin\theta(U_r' + c_r)}. \tag{9}$$

By using the definition of C_v [Eq. (5)], we can express $R_{\max}$ as follows:

$$R_{\max} = \sqrt{\frac{V_{\max}}{2\pi\beta C_v}}. \tag{10}$$

Substituting $R_{\max}$ in Eq. (9) with Eq. (10), we obtain

$$\frac{\partial V_{\max}}{\partial t} = -\sqrt{\frac{\beta V_{\max}}{2\pi C_v}}\overline{\sin\theta(U_r' + c_r)}. \tag{11}$$

For the tendency of $V_{\max}$ at the initial time step, Eq. (11) can be written as

$$\frac{\partial V_{\max}}{\partial t} = -\sqrt{\frac{\beta V_{\max,0}}{2\pi C_{v,0}}}\overline{\sin\theta(U_r' + c_r)}. \tag{12}$$

Thus, we can derive the tendency of $\tilde{V}_{\max}$ by dividing both sides of Eq. (12) with $V_{\max,0}$, yielding

$$\frac{\partial \tilde{V}_{\max}}{\partial t} = -\sqrt{\frac{\beta}{2\pi V_{\max,0} C_{v,0}}}\overline{\sin\theta(U_r' + c_r)}. \tag{13}$$

Subsequently, considering that the lhs of Eq. (13) can be reasonably approximated as the average decreasing rate of $\tilde{V}_{\max}$ over the initial 5 days, we assume that $F_{\max}$ is proportional to the initial tendency of $\tilde{V}_{\max}$:

$$F_{\max} \propto \frac{\partial \tilde{V}_{\max}}{\partial t} = -\sqrt{\frac{\beta}{2\pi V_{\max,0} C_{v,0}}}\overline{\sin\theta(U_r' + c_r)} \propto -\sqrt{\frac{1}{C_{v,0}}}. \tag{14}$$

This derivation yields the $-C_{v,0}^{-1/2}$ dependence seen in our experimental results above. However, both β and $V_{\max,0}$ are also included in Eq. (14). While β changes only minimally in our experiments, $V_{\max,0}$ spans a wide range, which indicates that our prediction that only considers $C_{v,0}$ is an incomplete one. Meanwhile, variations in $\overline{\sin\theta(U_r' + c_r)}$, which represents azimuthal variations in the eddy radial flow, hold potential significance and might offset the influence of $V_{\max,0}$ term. As this eddy radial flow term lacks its own analytical framework, its evaluation within this context is not feasible and is instead characterized by the parameter α in Eq. (7). Ultimately, the fitted prediction curve explains the majority of variance in Fig. 5, which means that $F_{\max}$ is dominated by $-C_{v,0}^{-1/2}$, while β and $V_{\max,0}$ may induce additional secondary effects on the intensity evolution that is stronger for incompact vortices.

5. Conclusions and discussion

This study aims to investigate the influence of planetary Rossby wave drag on TC seed vortex intensity and its sensitivity to vortex structure. The following key findings have been established:

- Vortex structural compactness (C_v) is defined as the ratio between vortex intensity ($V_{\max}$) and the Rhines speed (U_{Rh}) at the radius of maximum wind ($R_{\max}$), serving as an indicator of planetary Rossby wave drag's impact on $V_{\max}$.
- Considering planetary Rossby wave drag as the sole vorticity sink, the initial C_v ($C_{v,0}$) of a vortex exhibits a direct correlation with the strength of this wave drag on $V_{\max}$. Hence, $C_{v,0}$ has been established as a reliable predictor of the vortex weakening rate ($F_{\max}$) induced by planetary Rossby wave drag.
- The analysis of *VARYRVMAX* and *RANKINE* demonstrates the accurate prediction of $F_{\max}$ in idealized axisymmetric vortices on a barotropic β plane based on its initial $C_{v,0}$.
- The experiment sets *ASYMSEED* and *SYMSEED* further validate the applicability of our structural compactness theory to realistic vortices.
- In both *ASYMSEED*, where realistic 2D axis-asymmetry is included, and *SYMSEED*, which removes this axis-asymmetry from the realistic seed vortex, the relationship between $C_{v,0}$ and $F_{\max}$ remains relatively unchanged though *SYMSEED* exhibits a more robust $C_{v,0}$–$F_{\max}$ relationship.
- In *LARGESEED*, we decrease seed vortices' $C_{v,0}$ by manually enlarging the entire vortex without altering other features, and the results yield a similar relationship between $C_{v,0}$ and $F_{\max}$.
- The weakening rate in our experiments closely follows a $-C_{v,0}^{-1/2}$ dependence and is particularly robust when the vortex is initially compact ($C_{v,0} > 1$). For incompact cases, the eddy term likely drives additional variability but lacks a simple theoretical explanation.

In conclusion, the comprehensive experiment sets conducted on the barotropic β plane provide robust evidence supporting the proposition that vortex structural compactness serves as a reliable predictor of the rate at which the vortex weakens due to planetary Rossby wave drag. A TC seed vortex with a compact structure (higher C_v) experiences less planetary Rossby wave drag at the radius of $V_{\max}$ and, consequently, has the potential to persist longer compared to a

seed with an incompact structure (lower C_v) under similar environmental conditions.

Across all of our experiment sets, even when a vortex possesses a C_v value greater than 1, it still experiences weakening due to planetary Rossby wave drag. This observation underscores the fact that the dynamical pouch does not function as an impervious barrier that entirely shields V_{max} from stimulating planetary Rossby waves. In fact, planetary Rossby waves can be stimulated even when the circulation is within the dynamical pouch. However, due to the relatively short circulation time scale within the dynamical pouch, the vortex's circulation is able to self-advect before being significantly affected by planetary Rossby wave drag, resulting in less weakening of the circulation. Consequently, if a vortex exhibits a C_v value that is not significantly larger than 1, self-advection at R_{max} is comparable in magnitude to planetary Rossby wave drag, albeit slightly greater. As a result, the vortex will weaken due to planetary Rossby wave drag, while the weakening rate is much slower than those incompact vortices ($C_v < 1$).

The parameter C_v proposed in this study has important practical applications, particularly in the context of TC seed dynamics on Earth. It plays a crucial role in determining a seed vortex's ability to resist significant drag by planetary Rossby waves, especially in the tropics. The requirement to maintain compactness in the seed vortex imposes limitations on its representation in weather and climate modeling. For instance, when employing a global model with coarser horizontal resolution, the smaller values of R_{max} and stronger magnitudes of V_{max} associated with a compact seed vortex may not be adequately resolved. Consequently, the model might underestimate the seed's C_v, leading to an overestimation of planetary Rossby wave drag and predicting a faster weakening for the seed. This may explain why lower-resolution models tend to produce far fewer tropical cyclones than observed (Yamada et al. 2021; Sobel et al. 2021; Roberts et al. 2020; Murakami and Sugi 2010). Ensuring accurate representation of compactness becomes essential in such modeling scenarios to obtain reliable predictions for TC seed evolution.

While we utilize a realistic TC seed structure obtained from ERA5 to initialize our barotropic model and examine the rate of vortex weakening, it is important to note that our results do not directly represent the actual V_{max} evolution of the seed in reanalysis data. The parameter C_v, as demonstrated in the preceding section, solely captures the influence of planetary Rossby wave drag on V_{max}, disregarding other physical processes, particularly the vorticity source term due to vortex stretching from convection (Hsieh et al. 2020), that may potentially impact vortex intensity. Future work seeking to understand TC seeds in the real world should examine the competing effects of both source and sink terms of vorticity. Beyond the barotropic aspect, previous studies have highlighted various structural features that may influence the evolution of vortex intensity in more realistic scenarios. For instance, the radial structure of tangential winds within a vortex can impact the radial distribution of inertial stability, thereby affecting the rate of intensification (Schubert and Hack 1982; Wang and Xu 2010; Rogers et al. 2013; Pendergrass and Willoughby 2009; Chen et al. 2011). Furthermore, *f*-plane simulation studies (Xu and Wang 2018; Tao et al. 2020) have shown that vortices with a larger R_{max} tend to intensify more slowly. These findings collectively suggest that, in addition to planetary Rossby wave drag, numerous mechanisms can influence the intensification of a seed vortex. This indicates the need for future research to compare the effects of planetary Rossby wave drag with these other mechanisms comprehensively to enhance our understanding of TC seed development.

Several aspects of this subject remain unresolved, warranting further investigation. While our theory and experimental results indicate the importance of C_v as a parameter for examining the evolution of vortex intensity, the factors governing the evolution of vortex structural compactness remain uncertain. The underlying causes behind the comparatively less robust prediction of F_{max} for incompact vortices remain uncertain. Further exploration is needed to delve into the potential influence of other variations in vortex structure on this phenomenon. Additionally, since this study only investigated the structure of developing seeds, it remains uncertain whether nondeveloping seeds statistically possess a less compact structure compared to developing seeds. Addressing these questions requires modeling the development of TC seeds and conducting a comprehensive survey that includes both developing and nondeveloping seeds to better understand the interplay between TC seed structure and intensity. By investigating these aspects, we can gain deeper insights into the dynamics and behavior of TC seeds, which may lead to advancements in our understanding of TC genesis and frequency.

Acknowledgments. The authors thank Tim Cronin for introducing us to the concept of wave drag. Thank James Penn and Geoffrey K. Vallis for posting their barotropic model code publicly. Funding support was provided by NSF Grant 1945113.

Data availability statement. The IBTrACS dataset can be accessed publicly at https://doi.org/10.25921/82ty-9e16. The best track dataset (IBTrACS) can be accessed at https://www.ncei.noaa.gov/products/international-best-track-archive. The ERA5 data are openly available from the C3S Climate Data Store (e.g., https://doi.org/10.24381/cds.bd0915c6; https://doi.org/10.24381/cds.f17050d7; https://doi.org/10.24381/cds.6860a573). Data and scripts for figures in this paper are available on PURR: https://doi.org/10.4231/GV7J-6Z90.

APPENDIX

Derivation of the Rhines Number

As stated in the main body of the text, the simplest system for examining the interaction between a vortex and planetary Rossby wave drag is a single-layer barotropic vorticity equation:

$$\frac{\partial \zeta}{\partial t} = -\mathbf{u} \cdot \nabla \zeta - \beta v. \tag{A1}$$

All notations in Eq. (A1) correspond to those in Eq. (2). To determine which term on the RHS dominates the vorticity tendency of a vortex, a scale analysis is conducted within a cylindrical coordinate framework. First, the relative vorticity ζ is defined as the sum of the radial gradient of the tangential wind (shear vorticity) and the ratio of the tangential

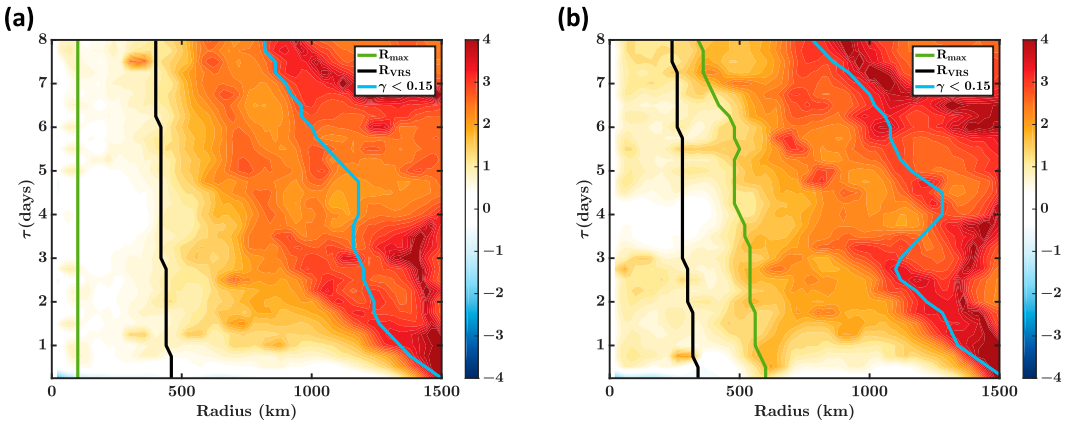

FIG. A1. Hovmöller diagrams illustrate the evolution of ε_{Rh} across two example experiment members. (a) An experiment member from *RANKINE* that has a compact vortex with an initial $V_{max} = 50$ m s^{-1} at $R_{max} = 100$ km. The contours represent the temporal radial distribution of ε_{Rh}. The green curve indicates R_{max}, the black curve indicates R_{VRS}, and the light blue curve indicates the radius at which the axisymmetricity, γ, is less than 0.15. (b) As in (a), but for an experiment member from *RANKINE* that has an incompact vortex with an initial $V_{max} = 20$ m s^{-1} at $R_{max} = 300$ km.

wind to the circulation radius (curvature vorticity). Consequently, the vorticity may be scaled by U_c/r, where U_c represents the azimuthally averaged tangential wind speed of this vortex and r denotes the radius of U_c. Next, the first term on the rhs of Eq. (A1) represents the nonlinear advection term. Given that a 2D barotropic fluid is nondivergent, it lacks an azimuthally averaged radial wind capable of advecting the radial gradient of vorticity. Here, for simplicity, we further assume that the scale of the nonlinear advection term is dominated by the tangential advection of the vorticity: $U_c \cdot \nabla_t \zeta$, where ∇_t represents the tangential gradient. Different from the radial gradient, which is scaled by $1/r$, the tangential gradient is scaled by $1/2\pi r$. Hence, the nonlinear advection term can be scaled by $U_c^2/(2\pi r^2)$. Last, the second term on the RHS of Eq. (A1) is β term, representing the meridional wind advecting β. Considering an environment with no background flow and assuming the vortex mean circulation is the only source of the meridional flow, β term can be scaled by βU_c. With these assumptions, we can scale each term in Eq. (A1) with vortex parameters on a cylindrical coordinate:

$$\frac{U_c}{rT} = -\frac{U_c^2}{2\pi r^2} - \beta U_c, \tag{A2}$$

where T represents the circulation time scale.

To determine which term on the RHS of Eq. (A1) dominates the vorticity tendency, we define the ratio between the nonlinear advection term and the β term as the Rhines number (Rh). Combined with Eq. (A2), we can approximate Rh as follows:

$$\frac{\mathbf{u}\cdot\nabla\zeta}{\beta v} \equiv \mathrm{Rh} \approx \frac{\frac{U_c^2}{2\pi r^2}}{\beta U_c} = \frac{U_t}{2\pi\beta r^2}. \tag{A3}$$

For a circulation with a known wind speed and radius that yields Rh $\gg$ 1, its vorticity tendency is dominated by the nonlinear advection term. This indicates that this circulation has less planetary Rossby wave drag on it. Conversely, for a circulation with Rh $\ll$ 1, its vorticity tendency is dominated by β term, which indicates that this circulation has more planetary Rossby wave drag on it.

Note that the sole approximation employed in this derivation is neglecting the eddy flow. Consequently, the theoretical Rh as predicted by Eq. (A3) is expected to exhibit significant negative bias, particularly in scenarios where the circulation demonstrates a high degree of axis-asymmetry. To demonstrate the distribution of this bias, a comparison of the first and final terms in Eq. (A3) can be conducted within the context of our barotropic experiments. Given that the first term in Eq. (A3) represents the physical definition of the Rh and can be directly outputted from the barotropic model, it is designated as $\mathrm{Rh}_{\mathrm{Real}}$. On the other hand, since the final term in Eq. (A3) is derived based on theoretical approximations, it is defined as $\mathrm{Rh}_{\mathrm{Theory}}$. To better quantify the discrepancy between $\mathrm{Rh}_{\mathrm{Real}}$ and $\mathrm{Rh}_{\mathrm{Theory}}$, we introduce the concept of the Rhines number discrepancy ($\varepsilon_{\mathrm{Rh}}$) as follows:

$$\varepsilon_{\mathrm{Rh}} = \log_{10}\left(\frac{\mathrm{Rh}_{\mathrm{Real}}}{\mathrm{Rh}_{\mathrm{Theory}}}\right) = \log_{10}\left(\frac{\mathbf{u}\cdot\nabla\zeta/\beta v}{U_t/2\pi\beta r^2}\right). \tag{A4}$$

A larger value of $\varepsilon_{\mathrm{Rh}}$ indicates that $\mathrm{Rh}_{\mathrm{Real}}$ is significantly larger than $\mathrm{Rh}_{\mathrm{Theory}}$, suggesting a greater negative bias in the theoretical Rh.

Figure A1 illustrates the evolution of $\varepsilon_{\mathrm{Rh}}$ for two example members from *RANKINE*. In Fig. A1a, which shows a vortex with an initially compact structure, the area exhibiting higher values of $\varepsilon_{\mathrm{Rh}}$ is predominantly located outside R_{VRS} (represented by the black curve, which indicates the radius where $\mathrm{Rh}_{\mathrm{Theory}} = 1$). Furthermore, the highest values of $\varepsilon_{\mathrm{Rh}}$ are observed in regions of high axis-asymmetry, specifically beyond the light blue curve. It is noteworthy that R_{VRS} is located in a region characterized by a relatively low value of $\varepsilon_{\mathrm{Rh}}$ (approximately below 1), suggesting

that using Rh_{Theory} to define R_{VRS} is robust. Moreover, the R_{max} of this vortex, as indicated by the green curve, consistently falls within a region exhibiting a lower value of ε_{Rh}. This observation also supports the notion that for an initially compact vortex, C_v, which is defined as Rh_{Theory} evaluated at R_{max}, can accurately reflect Rh_{Real} at R_{max}. On the other hand, in Fig. A1b, which shows a vortex with an initially incompact structure, its R_{max} is initially outside R_{VRS} and falls within a region that has a higher ε_{Rh} compared to Fig. A1a. This suggests that C_v of an incompact vortex tends to underestimate its R_{Real} at R_{max}, thereby highlighting a reduced robustness in the C_v–F_{max} relationship among initially incompact members.

REFERENCES

Asaadi, A., G. Brunet, and M. K. Yau, 2016a: On the dynamics of the formation of the Kelvin cat's-eye in tropical cyclogenesis. Part I: Climatological investigation. *J. Atmos. Sci.*, **73**, 2317–2338, https://doi.org/10.1175/JAS-D-15-0156.1.

——, ——, and ——, 2016b: On the dynamics of the formation of the Kelvin cat's-eye in tropical cyclogenesis. Part II: Numerical simulation. *J. Atmos. Sci.*, **73**, 2339–2359, https://doi.org/10.1175/JAS-D-15-0237.1.

——, ——, and ——, 2017: The importance of critical layer in differentiating developing from nondeveloping easterly waves. *J. Atmos. Sci.*, **74**, 409–417, https://doi.org/10.1175/JAS-D-16-0085.1.

Cao, X., G. Chen, and W. Chen, 2013: Tropical cyclogenesis induced by ITCZ breakdown in association with synoptic wave train over the western North Pacific. *Atmos. Sci. Lett.*, **14**, 294–300, https://doi.org/10.1002/asl2.452.

Chavas, D. R., 2022: Code for tropical cyclone wind profile model of Chavas et al (2015, JAS). Purdue University Research Repository, accessed 6 June 2022, https://doi.org/10.4231/CZ4P-D448.

——, N. Lin, and K. Emanuel, 2015: A model for the complete radial structure of the tropical cyclone wind field. Part I: Comparison with observed structure. *J. Atmos. Sci.*, **72**, 3647–3662, https://doi.org/10.1175/JAS-D-15-0014.1.

Chen, D. Y.-C., K. K. W. Cheung, and C.-S. Lee, 2011: Some implications of core regime wind structures in western North Pacific tropical cyclones. *Wea. Forecasting*, **26**, 61–75, https://doi.org/10.1175/2010WAF2222420.1.

Cronin, T. W., and D. R. Chavas, 2019: Dry and semidry tropical cyclones. *J. Atmos. Sci.*, **76**, 2193–2212, https://doi.org/10.1175/JAS-D-18-0357.1.

Dunkerton, T. J., M. T. Montgomery, and Z. Wang, 2009: Tropical cyclogenesis in a tropical wave critical layer: Easterly waves. *Atmos. Chem. Phys.*, **9**, 5587–5646, https://doi.org/10.5194/acp-9-5587-2009.

Emanuel, K., 2005: Increasing destructiveness of tropical cyclones over the past 30 years. *Nature*, **436**, 686–688, https://doi.org/10.1038/nature03906.

——, and R. Rotunno, 2011: Self-stratification of tropical cyclone outflow. Part I: Implications for storm structure. *J. Atmos. Sci.*, **68**, 2236–2249, https://doi.org/10.1175/JAS-D-10-05024.1.

Haynes, P. H., and M. E. McIntyre, 1987: On the evolution of vorticity and potential vorticity in the presence of diabatic heating and frictional or other forces. *J. Atmos. Sci.*, **44**, 828–841, https://doi.org/10.1175/1520-0469(1987)044%3C0828:OTEOVA%3E2.0.CO;2.

Held, I. M., and M. Zhao, 2008: Horizontally homogeneous rotating radiative–convective equilibria at GCM resolution. *J. Atmos. Sci.*, **65**, 2003–2013, https://doi.org/10.1175/2007JAS2604.1.

Hoogewind, K. A., D. R. Chavas, B. A. Schenkel, and M. E. O'Neill, 2020: Exploring controls on tropical cyclone count through the geography of environmental favorability. *J. Climate*, **33**, 1725–1745, https://doi.org/10.1175/JCLI-D-18-0862.1.

Hopsch, S. B., C. D. Thorncroft, and K. R. Tyle, 2010: Analysis of African Easterly wave structures and their role in influencing tropical cyclogenesis. *Mon. Wea. Rev.*, **138**, 1399–1419, https://doi.org/10.1175/2009MWR2760.1.

Hsieh, T.-L., G. A. Vecchi, W. Yang, I. M. Held, and S. T. Garner, 2020: Large-scale control on the frequency of tropical cyclones and seeds: A consistent relationship across a hierarchy of global atmospheric models. *Climate Dyn.*, **55**, 3177–3196, https://doi.org/10.1007/s00382-020-05446-5.

Ikehata, K., and M. Satoh, 2021: Climatology of tropical cyclone seed frequency and survival rate in tropical cyclones. *Geophys. Res. Lett.*, **48**, e2021GL093626, https://doi.org/10.1029/2021GL093626.

Kieu, C. Q., and D.-L. Zhang, 2008: Genesis of Tropical Storm Eugene (2005) from merging vortices associated with ITCZ breakdowns. Part I: Observational and modeling analyses. *J. Atmos. Sci.*, **65**, 3419–3439, https://doi.org/10.1175/2008JAS2605.1.

Klotzbach, P. J., D. R. Chavas, M. M. Bell, S. G. Bowen, E. J. Gibney, and C. J. Schreck III, 2022: Characterizing continental US hurricane risk: Which intensity metric is best? *J. Geophys. Res. Atmos.*, **127**, e2022JD037030, https://doi.org/10.1029/2022JD037030.

Knapp, K. R., M. C. Kruk, D. H. Levinson, H. J. Diamond, and C. J. Neumann, 2010: The International Best Track Archive for Climate Stewardship (IBTrACS): Unifying tropical cyclone data. *Bull. Amer. Meteor. Soc.*, **91**, 363–376, https://doi.org/10.1175/2009BAMS2755.1.

Lee, C.-Y., S. J. Camargo, A. H. Sobel, and M. K. Tippett, 2020: Statistical–dynamical downscaling projections of tropical cyclone activity in a warming climate: Two diverging genesis scenarios. *J. Climate*, **33**, 4815–4834, https://doi.org/10.1175/JCLI-D-19-0452.1.

Lu, K.-Y., and D. R. Chavas, 2022: Tropical cyclone size is strongly limited by the Rhines scale: Experiments with a barotropic model. *J. Atmos. Sci.*, **79**, 2109–2124, https://doi.org/10.1175/JAS-D-21-0224.1.

Murakami, H., and M. Sugi, 2010: Effect of model resolution on tropical cyclone climate projections. *SOLA*, **6**, 73–76, https://doi.org/10.2151/sola.2010-019.

Nolan, D. S., E. D. Rappin, and K. A. Emanuel, 2007: Tropical cyclogenesis sensitivity to environmental parameters in radiative–convective equilibrium. *Quart. J. Roy. Meteor. Soc.*, **133**, 2085–2107, https://doi.org/10.1002/qj.170.

Pendergrass, A. G., and H. E. Willoughby, 2009: Diabatically induced secondary flows in tropical cyclones. Part I: Quasi-steady forcing. *Mon. Wea. Rev.*, **137**, 805–821, https://doi.org/10.1175/2008MWR2657.1.

Persing, J., M. T. Montgomery, and R. E. Tuleya, 2002: Environmental interactions in the GFDL hurricane model for Hurricane Opal. *Mon. Wea. Rev.*, **130**, 298–317, https://doi.org/10.1175/1520-0493(2002)130%3C0298:EIITGH%3E2.0.CO;2.

Rappaport, E. N., 2014: Fatalities in the United States from Atlantic tropical cyclones: New data and interpretation. *Bull.*

Amer. Meteor. Soc., **95**, 341–346, https://doi.org/10.1175/BAMS-D-12-00074.1.

Raymond, D. J., and C. López Carrillo, 2011: The vorticity budget of developing Typhoon Nuri (2008). *Atmos. Chem. Phys.*, **11**, 147–163, https://doi.org/10.5194/acp-11-147-2011.

Roberts, M. J., and Coauthors, 2020: Impact of model resolution on tropical cyclone simulation using the HighResMIP–PRIMAVERA multimodel ensemble. *J. Climate*, **33**, 2557–2583, https://doi.org/10.1175/JCLI-D-19-0639.1.

Rogers, R., P. Reasor, and S. Lorsolo, 2013: Airborne Doppler observations of the inner-core structural differences between intensifying and steady-state tropical cyclones. *Mon. Wea. Rev.*, **141**, 2970–2991, https://doi.org/10.1175/MWR-D-12-00357.1.

Russell, J. O., A. Aiyyer, J. D. White, and W. Hannah, 2017: Revisiting the connection between African Easterly waves and Atlantic tropical cyclogenesis. *Geophys. Res. Lett.*, **44**, 587–595, https://doi.org/10.1002/2016GL071236.

Schubert, W. H., and J. J. Hack, 1982: Inertial stability and tropical cyclone development. *J. Atmos. Sci.*, **39**, 1687–1697, https://doi.org/10.1175/1520-0469(1982)039<1687:ISATCD>2.0.CO;2.

Shimada, U., K. Aonashi, and Y. Miyamoto, 2017: Tropical cyclone intensity change and axisymmetricity deduced from GSMaP. *Mon. Wea. Rev.*, **145**, 1003–1017, https://doi.org/10.1175/MWR-D-16-0244.1.

Smith, K. S., G. Boccaletti, C. C. Henning, I. Marinov, C. Y. Tam, I. M. Held, and G. K. Vallis, 2002: Turbulent diffusion in the geostrophic inverse cascade. *J. Fluid Mech.*, **469**, 13–48, https://doi.org/10.1017/S0022112002001763.

Smith, R. K., H. C. Weber, and A. Kraus, 1995: On the symmetric circulation of a moving hurricane. *Quart. J. Roy. Meteor. Soc.*, **121**, 945–952, https://doi.org/10.1002/qj.49712152412.

Sobel, A. H., A. A. Wing, S. J. Camargo, C. M. Patricola, G. A. Vecchi, C.-Y. Lee, and M. K. Tippett, 2021: Tropical cyclone frequency. *Earth's Future*, **9**, e2021EF002275, https://doi.org/10.1029/2021EF002275.

Sugi, M., Y. Yamada, K. Yoshida, R. Mizuta, M. Nakano, C. Kodama, and M. Satoh, 2020: Future changes in the global frequency of tropical cyclone seeds. *SOLA*, **16**, 70–74, https://doi.org/10.2151/sola.2020-012.

Tang, B., and S. J. Camargo, 2014: Environmental control of tropical cyclones in CMIP5: A ventilation perspective. *J. Adv. Model. Earth Syst.*, **6**, 115–128, https://doi.org/10.1002/2013MS000294.

Tao, D., M. Bell, R. Rotunno, and P. J. van Leeuwen, 2020: Why do the maximum intensities in modeled tropical cyclones vary under the same environmental conditions? *Geophys. Res. Lett.*, **47**, e2019GL085980, https://doi.org/10.1029/2019GL085980.

Thorncroft, C., and K. Hodges, 2001: African easterly wave variability and its relationship to Atlantic tropical cyclone activity. *J. Climate*, **14**, 1166–1179, https://doi.org/10.1175/1520-0442(2001)014%3C1166:AEWVAI%3E2.0.CO;2.

Vecchi, G. A., and Coauthors, 2019: Tropical cyclone sensitivities to CO_2 doubling: Roles of atmospheric resolution, synoptic variability and background climate changes. *Climate Dyn.*, **53**, 5999–6033, https://doi.org/10.1007/s00382-019-04913-y.

Vennell, R., D. Pease, and B. Wilson, 2006: Wave drag on human swimmers. *J. Biomech.*, **39**, 664–671, https://doi.org/10.1016/j.jbiomech.2005.01.023.

Vorontsov, A., and V. A. Rumyantsev, 2000: Propulsive forces in swimming. *Biomechanics in Sport: Performance Enhancement and Injury Prevention*, V. M. Zatsiorsky, Ed., Wiley, 205–231.

Wang, Y., and J. Xu, 2010: Energy production, frictional dissipation, and maximum intensity of a numerically simulated tropical cyclone. *J. Atmos. Sci.*, **67**, 97–116, https://doi.org/10.1175/2009JAS3143.1.

Wilson, B., and R. Thorp, 2003: Active drag in swimming. *Biomechanics and Medicine in Swimming IX*, Publications de l'Université de Saint Etienne, 15–20.

Wing, A. A., S. J. Camargo, and A. H. Sobel, 2016: Role of radiative–convective feedbacks in spontaneous tropical cyclogenesis in idealized numerical simulations. *J. Atmos. Sci.*, **73**, 2633–2642, https://doi.org/10.1175/JAS-D-15-0380.1.

Xu, J., and Y. Wang, 2018: Effect of the initial vortex structure on intensification of a numerically simulated tropical cyclone. *J. Meteor. Soc. Japan*, **96**, 111–126, https://doi.org/10.2151/jmsj.2018-014.

Yamada, Y., and Coauthors, 2021: Evaluation of the contribution of tropical cyclone seeds to changes in tropical cyclone frequency due to global warming in high-resolution multi-model ensemble simulations. *Prog. Earth Planet. Sci.*, **8**, 11, https://doi.org/10.1186/s40645-020-00397-1.

Yang, C., F. Huang, and F. Noblesse, 2013: Practical evaluation of the drag of a ship for design and optimization. *J. Hydrodyn.*, **25**, 645–654, https://doi.org/10.1016/S1001-6058(13)60409-6.